



Observational signatures of charged rotating traversable wormhole: shadows and light rings with different accretions

Rabia Saleem^a, M. Israr Aslam^b, Shokaib Shahid^c

Department of Mathematics, COMSATS University Islamabad, Lahore-Campus, Lahore 54000, Pakistan

Received: 2 December 2023 / Accepted: 25 April 2024
© The Author(s) 2024

Abstract In this work, we investigate the optical appearance of qualitatively new observational features of accretion disk images around the charged rotating traversable wormhole (TWH) space-time for different spin, throat, and charge values. To accomplish this, we first consider the Hamilton–Jacobi method to derive the geodesic equations for the motion of photons and study the effects of parameters on the photon orbit in the observer’s sky. We found that each parameter affects the size and shape of the wormhole (WH) shadow and flatness is observed in the shadow because of spin and other parameters. To produce shadow images of sufficient visual quality but within manageable computational times, we adopt the ray-trace procedure and characterize the significant features of light trajectories on the observer’s screen, depending on the interaction between the space-time structure and the accretion disk. In addition, we consider the static spherically symmetric accretion flow model to observe the specific intensity around the traversable WH space-time geometry. It is found that the intensity and positions of the photon ring vary with respect to the involved parameters. In future observation, this type of study may provide a fertile playground to test the nature of compact objects, specifically the WH in the strong-field regime.

1 Introduction

During the last two decades, the expanding nature of our universe has been described by a large amount of recent observational data such as Laser Interferometer Gravitational Wave Observatory [1], Virgo [2], Event Horizon Telescope (EHT) [3], International Gamma-Ray Astrophysics Laboratory [4]

and Imaging X-ray Polarimetry mission [5]. These observations triggered the research community to investigate and develop more insights and advanced techniques to test gravity in a strong gravitational regime. Wormhole (WHs) is a theoretical solution of Einstein’s field equations that has no horizon or singularity. Theoretically, WHs are hypothetical objects connecting two distinct points in the same or even different universes by speed more than light. Wormholes have never been observed and even their existence and formation scenarios are highly disputable questions.

In 1916, Flamm was the first, who proposed the theoretical formulation of WHs [6]. Later in 1935, Einstein and Rosen [7] developed the inevitable results in the formation of WHs, which connected two different mouths of Schwarzschild geometry. Since the TWHs do not take into observation, it was thought that they were just a mathematical prediction at this time. The existence of human TWHs requires gravitational repulsion, which usually could be supported by matter with negative kinetic terms, restraining the throat from shrinking. The traditional method that is used to find the WH solutions entails creating a singularity-free metric that shows the proper WH geometry, which needs some exotic matter at the throat to keep it open. By applying this strategy, Morris and Thorne [8] investigated the static TWHs without time dependence and came to the conclusion that they couldn’t be created through the usual matter. There is a stress-energy tensor that is present in all known classical forms of matter and meets specific energy requirements [9].

In this scenario, Morris–Thorne WHs must include the matter whose stress-energy tensor violates the null energy condition, and hence all the solutions of Einstein field equations are valid. Subsequently, the solutions of rotating axially symmetric TWHs were also discovered in [10] along with those that had time-dependent angular velocity [11]. Since the possible characteristics of the TWHs were studied for a long time, many developments were carried out

^a e-mail: rabiasaleem@cuilahore.edu.pk (corresponding author)

^b e-mail: mrisraraslam@gmail.com

^c e-mail: sshokaib86@gmail.com

by various researchers. Further, it is generally accepted that super-massive compact objects, most frequently thought to be black holes (BHs), are present in the galactic centers. Boson stars, gravastars, and WHs are examples of horizonless objects, however, they cannot yet be completely ruled out. As a result, it's critical to consider tests that can discriminate between WHs and BH for upcoming observations.

Among various objects in gravitational physics, the most peculiar astrophysical objects are the BH and WH. Gravitational lensing is one of the fundamental phenomena of strong gravity. The observation in 2019 by the EHT [12–14] of the accretion flow around the super-massive object at the center of *M87** has triggered the beginning of a new phase in the understanding of the magnetic fields around compact objects and on testing general relativity (GR) itself. In these papers, the concepts of BH shadow depicted a bright ring-shaped lump of radiation surrounding a black central region of an estimated 6.5 billion solar masses. In this sense, the research on the BH shadows has entered a new phase, which provides the details of the astrophysical circumstances of the accretion matter and its optical appearance in a general relativistic context [15]. In 2020, Kruglov [16] examined the rational nonlinear electrodynamics and described the super-massive *M87** BH as a magnetized BH without singularities. The shadow that was observed from the center of *M87** was consistent with the shadow produced by numerical simulation of a Kerr-like BH with a mass of ($M = 6.5 \pm 0.7 \times 10^9 M_{\odot}$) (where M is the mass of BH) [15]. The details of the accretion process and emission mechanisms influence the intensity map of an image, but the boundary of the shadow relies solely on the space-time metric. This is because the shadow boundary reflects the apparent shape of the photon orbits, which can be observed by any distant observer.

Since the visual appearance of BH shadows is widely discussed in the literature, it prompts us to better understand the realistic nature of plasma radiation around the BH. In 1999, Falcke et al. [17] proposed that the BH shadow is equivalent to the gravitational lensing effect by assuming the accretion flow is optically thin surrounding a super-massive BH in the center of our Milky Way galaxy. In [18], the author proposed a technique that is used to determine the BH charge through the distinct features of BH shadow in the galactic center and found that this method is also valid when a BH is uncharged. Abdujabbarov et al. [19] studied the shadow of a charged rotating BH and concluded that the angular momentum of the BH deforms the size of the shadow according to the variations of parameters. Assuming an optically thin disk accretion flow model, Gralla et al. [20] discussed the BH shadow and the photon rings of Schwarzschild BH and found that the luminosity of the ring diverges logarithmically at the position of the photon ring. Zeng et al. [21] analyzed some interesting features of the charged four-dimensional Gauss–Bonnet BH, considering the strings clouds and non-

commutative (NC) geometry under different accretions flow models. Saleem and Aslam [22] investigated the optical features of a charged NC Kiselev BH through different configurations of accretion matter. They found that the size of the BH shadow and its related properties closely depend on the BH state parameters and space-time geometry.

Takahashi [23] conducted both qualitative and quantitative analysis of the shadow created by a rotating BH on an optically thick accretion disk and investigated its characteristics which depend on the angular momentum of the BH. Saha et al. [24] introduced the NC geometry for the Ayón-Beato and García BH metric and studied the effects of NC parameter θ , smeared mass $m(r)$ and smeared charge $q(r)$ on the silhouette of the BH shadow. Solanki and Perlick [25] obtained the precise analytical equations that describe the evolution of the photon sphere and the angular radius of the BH shadow within a specific Vaidya space-time. Övgün et al. [26] studied the shadow and the energy emission rate of a spherically symmetric BH under NC geometry in the framework of Rastall gravity. Although these studies can provide valuable information about compact objects such as BHs, they may not always be sufficient to determine the underlying object with certainty. In this regard, researchers are trying to explore WHs to acquire a perception of their geometrical structures. Apart from gravitational lensing effects, another possible method for probing WHs is the canonical interpretation of shadows. Hence, one can recognize the shadow of a WH in the strong gravitational field, an object having a photon sphere when illuminated by an accretion disk.

The shadow of a WH is the area where the throat of the WH stops the light rays coming from the other side of the throat. This may result in a special phenomenon such as a light ring located only on one side of the WH throat and there is no light ring on the other side of the throat. The optical appearance of this shadow zone is similar, much like the shadow of a BH, but it is different in shape and structure. Since the shape of WH is thought to be a hypothetical geometry that has not yet been seen or proven to exist, it is difficult to pinpoint exactly what makes up a WH shadow [27]. Therefore, apart from the study of the shape and size of shadows, the WH shadows and their observational characteristics were studied for a long time [28,29], but still there are thrust in the research community to explore the nature of plasma radiation around the WH throat more comprehensively. The optical appearance of WH shadow closely depends on the accretion matter and its proper visualization can provide evidence about the parameters as well as space-time geometry around the WH. Based on null geodesics, the boundary of the shadow can be resolved by the WH space-time metric itself, as it is associated with the shape of the photon orbits, which is observed by any distant viewer. In this perspective, one can analyze the behavior of light rays around the WH throat based on null geodesic equations and solve it numerically through an efficient procedure, so-called

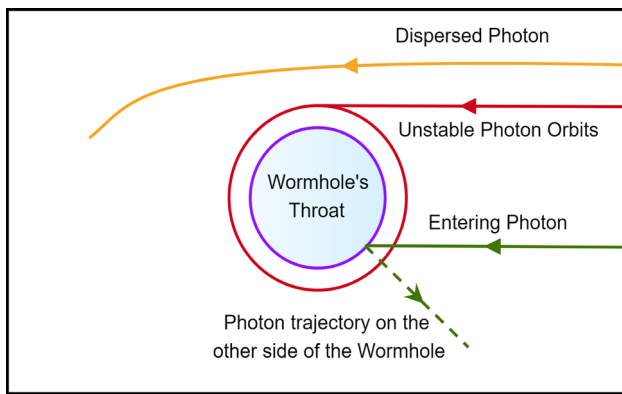


Fig. 1 Schematic diagram of the light rays around the WH

the ray-tracing method [30]. In this way, for a greater depth of understanding of the behavior of light rays from cosmic accretion materials, one can analyze it through the schematic diagram, which shows the optical appearance of the incident light rays around WH throat (see Fig. 1).

Based on the geodesics analysis, one can classify the light rays into three different kinds of emissions on the equatorial plane as shown in Fig. 1. These light rays are used to distinguish the behavior of photons according to their motions around the WH throat as follows: (i) In this case, the photons approaching the throat from far away in the universe I and will reach the left-turning point and be traced backward (dispersed from the WH to infinity) (see orange line), (ii) at the position of the photon sphere, the photons will neither escape from the WH nor fall into the WH, and hence revolve around the WH throat in a state of constant rotation (see red line). In other words, if a photon starts its motion in universe I , it will cross the WH throat to universe II and reach the position of the photon ring from where it can either scatter back to infinity in universe I or travel further towards the universe II , (iii) and when the photons travel across all of the space-time, entering from the asymptotic universe I of space-time and escape from the other side of the asymptotic region II of space-time and vice versa (see green line). Motivated by these fundamental concepts, Nedkova et al. [31] investigated the distinct features of a particular class of rotating TWHs shadows within the framework of GR and found that the inclination angle of the remote observer and the angular momentum of the WH both changes the images of the shadows.

In [32], the author examined the shadows of a particular class of rotating TWHs and found the main rule of a rotating WH throat in the formation of shadow images. They further explored the influence of spin parameter on the shadows and compared the results with that of Kerr BH, which can be used to distinguish the shadows of WHs and BHs. Rahaman et al. [33] investigated the shadow of rotating WH through the null geodesics analysis and discussed the effects of WH

state parameters on the photon ring and the shadow size, which significantly varies according to the values of parameters. Abdujabbarov et al. [34] investigated the behavior of massless particles around the rotating WH in the presence of plasma radiations and discovered that the inner radius of photon's circular orbits around the WH throat is reduced with the increasing of the plasma parameters. The optical properties of the shadow images along with both null and massive particles for the charged Morris–Thorne WH are discussed in [35] for different values of the charge and the other state parameters. Javed et al. [36] derived the Gaussian optical curvature through the Gauss–Bonnet theorem and calculated the weak deflection angle and the shadow images of the Casimir WH under different values of the involved parameters. Ohgami and Sakai [37] studied the shadow of WH under the influence of a rotating dust flow field. They derived the steady-state solutions of slowly rotating dust through the relativistic Euler equations and found that the shape of the bright ring is distorted due to the rotation of dust fluid. The authors in [38] discussed the problems of deflection and scattering of light rays having zero gravitational mass under different accretions flow matter and concluded that the ray-tracing procedure gives efficient information about electromagnetic phenomena around the compact objects such as BHs and WHs.

However, the different optical signatures of WH shadows and their relevant consequences obtained the peak position among the scientific community, and numerous publications have been devoted to this subject. Still, there are many problematic configurations that need to be investigated for the proper visualization of accreting matter around the WH through the reliable method, which is based on null geodesic analysis. This paper is organized as follows. In Sect. 2, we briefly define the basic formalism of charged rotating TWH along necessary constraints on the space-time structure. In Sect. 3, the equations of motion for mass-less particles are developed with the Hamilton–Jacobi formalism, and shadow curves for the observer at different locations are discussed in the same section. A ray-tracing procedure is employed in Sect. 4 to observe different light ray trajectories around TWH configurations. The observed specific intensity based on the static accretion flow model is also discussed in the same section. Finally, we draw the conclusions and add discussions in the last section.

2 The charged rotating wormhole

The charged parameter can be applied to develop the models of various astrophysical objects of immense gravity by considering the relevant matter distributions. These models with charged parameters can successfully describe stellar objects' characteristics [39]. Understanding the charged parameters in astrophysical objects is essential for gaining significant

information about space-time structure, and it plays a crucial role in astrophysical research and the development of theoretical models. The magnetic fields associated with charged particles in accretion disks can lead to the formation of jets and other energetic phenomena around stellar objects. In this regard, the well-known axisymmetric space-time metric describing a class of rotating TWH, which is proposed by Toe in [10] and can be written with charge Q in the following form as [40,41]

$$ds^2 = -N^2 dt^2 + \left(1 - \frac{b}{r} + \frac{Q^2}{r^2}\right)^{-1} dr^2 + r^2 K^2 [d\theta^2 + \sin^2\theta (d\phi - \omega dt)^2], \tag{1}$$

where

$$N = \sqrt{1 - \frac{2M}{r} + \frac{Q^2}{r^2}}, \quad b(r) = \frac{r_0^2 + 2M(r - r_0)}{r},$$

$$\omega = \frac{2J}{r^3} = \frac{2aM^2}{r^3}, \quad K = 1, \tag{2}$$

in which $a = \frac{J}{M^2}$ is the spin parameter, J is the angular momentum, r_0 is the WH throat, $K(r, \theta)$ is a regular, positive and non-decreasing function, determining the proper radial distance $R = rK$ and ω shows the angular velocity of the WH. Further, the spherical polar coordinates (t, r, θ, ϕ) are defined as $-\infty < t < \infty$, $r_0 \leq r \leq \infty$, $0 \leq \theta \leq \pi$ and $0 \leq \phi \leq 2\pi$, and the metric functions N, b, K and ω closely depends on r and θ . If both ω and Q are equal to zero, then the metric given in Eq. (1) reduces to the Morris–Thorne WH metric, and for $Q = 0$ only, it is reduced to rotating TWH [33]. The function N is the redshift function of radial coordinate and its value is always finite everywhere used to determine how gravitational redshift behaves as an object falls into the gravitational field. The parameter b is the shape function, which is used to determine the shape of the WH and it must satisfy the following conditions, throat condition $b(r_0) = r_0$ and $b(r)$ should be less than r for $r > r_0$, and flaring-out condition at the throat $b'(r_0) < 1$ [10] (where prime denotes derivative with respect to r). To ensure that the metric is non-singular on the rotation axis $\theta = 0$ and $\theta = \pi$, the derivatives of N, K , and b with respect to θ should vanish on it. As a result, the considering metric denotes two identical regions joined together at the throat, $r = r_0 = b$, and the radial coordinates approach to physical infinity. Although various choices for the metric functions N, K, b , and ω can be adopted freely, we emphasize that all the solutions do not correspond to WH physics. One must describe the necessary restrictions for the regularity and the physical relevance of the WH solutions. So, we will evaluate our results according to the above mentioned conditions.

Now, we will continue with the concept of ergoregion in the context of WHs. Generally, for the metric signature $(-, +, +, +)$, the temporal component $g_{tt} < 0$. However,

for rotating space-times, g_{tt} can be made positive in some regions and these regions are called ergoregions. The boundary between the negative and positive g_{tt} , where $g_{tt} = 0$ is known as ergosurface. So, the ergoregion is the region between the event horizon or the WH throat and at the ergosurface $g_{tt} = 0$. One of the properties of ergoregion is that no massive particle can move in a direction opposite to the spin of the space-time. In the ergoregion, if a massive particle starts moving initially opposite to the spin, it will ultimately reverse its motion and align its motion in the direction of the spin. The ergoregion for the rotating WHs is defined as $g_{tt} = -(N^2 - \omega^2 r^2 \sin^2 \theta) \geq 0$. So, for the metric given in Eq. (1), the ergosurface defined as:

$$N^2 - \omega^2 r^2 K^2 \sin^2 \theta = 0. \tag{3}$$

For rotating WHs, the ergoregion exists around its throat, so it is not extended up to poles at $\theta = 0$ and $\theta = \pi$. The ergosphere must exist in between a critical angle θ_c and $\pi - \theta_c$, for all $0 < \theta_c \leq \frac{\pi}{2}$. Now θ_c can be determined at the throat of the WH from Eq. (3) as [32,42]

$$\sin \theta_c = \left| \frac{N_0}{\omega_0 r_0 K_0} \right|, \tag{4}$$

here the “0” in subscript shows that the results are evaluated at the throat of the WH. Moreover, the critical value a_c of the spin parameter a is calculated by the correspondence of $\sin \theta_c = 1$ or $\omega_c = N_0/r_0 K_0$. In our case, the critical value $a_c = 1.22984$ for the values $M = 1, r_0 = 2.2$ and $Q = 0.9$. Graphical analysis of the ergosphere for the given values using $a > a_c$ are shown in Fig. 2. From Fig. 2a, when we fixed the spin parameter $a = 1.3$, we observed that there is no significant difference between the WH throat and the ergosurface. Explicitly from Fig. 2a–d, as the strength of the spin parameter a increases, the distance between the ergosurface and the WH throat is expanded. Moreover, as the spin parameter a increases, the curves of the ergosurface lie far away from the WH throat. Further, we plotted the sub-figures of ergosphere for different values of Q as shown in the lower panel of Fig. 2, corresponding to different values of a as depicted in Fig. 2 (upper row). From these subfigures, we conclude that when the charge Q has a maximum value such as $Q = 0.8$, a very narrow gap between the ergosurface and the WH throat has been noticed (see Fig. 2e). Further, when the charge $Q = 0.6$ (see Fig. 2f), the corresponding profile shows that the distance between the ergosurface and the WH throat is gradually expanded. As the value of charge Q further drops, we notice a further increase in the distance between the ergosurface and the WH throat. Hence, all these results imply that the position of the ergosurface with respect to the throat closely depends on the state parameters. In general, the distance between the ergosurface and the throat is changed according to the relative locations of objects and

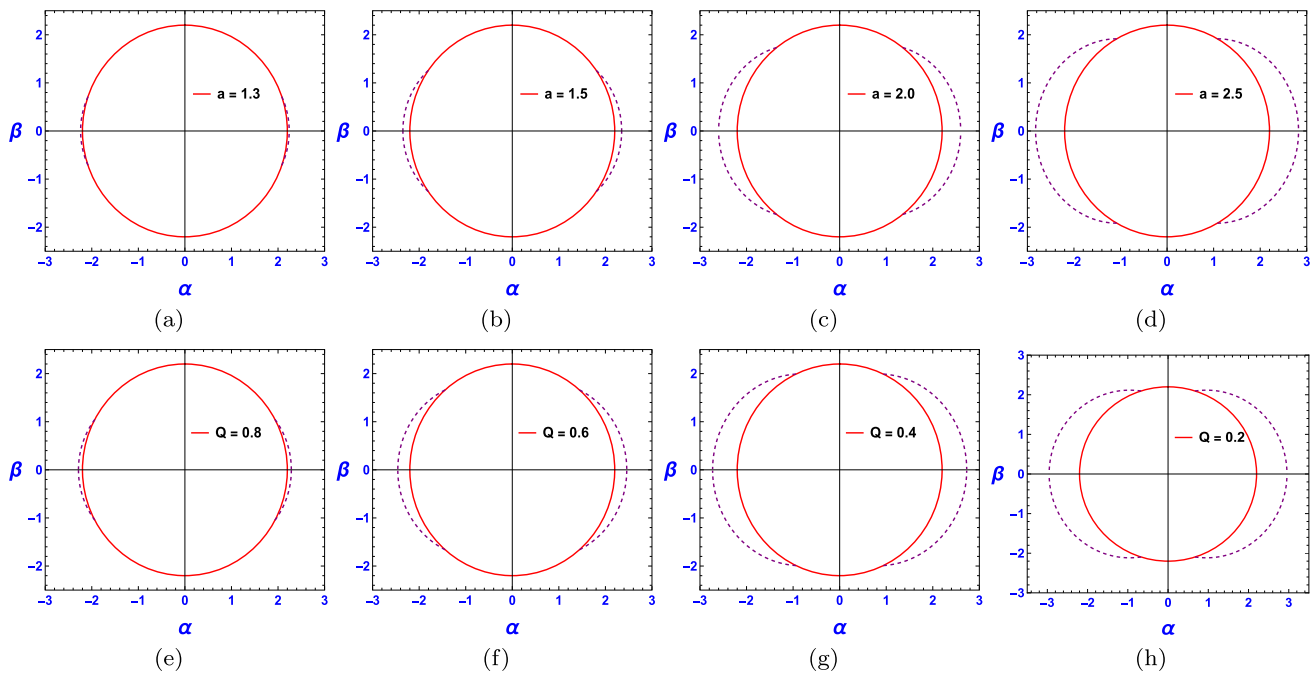


Fig. 2 The figure shows the ergosphere for different values of a (upper panel) and for different Q (lower panel). The ergoregion is limited to a crescent-shaped region about the equator and is denoted by a purple-dashed curve. The red line represents the WH throat at $r = r_0$

their geometrical properties. As objects move in the vicinity of a WH, the ergosurface may shift accordingly.

3 Motion of mass-less particles

To investigate the behavior of light rays around the charged rotating TWHs, we need to find how the light ray moves in this space-time. To study the shadow and its relevant consequences for rotating metrics in a strong field regime, we need to define the geodesic equations, which are defined through the Hamilton–Jacobi formulation [43,44]. The dynamics of mass-less particles are widely discussed in the literature with the help of Lagrangian and Hamiltonian formalism in the context of modified theories of gravity [45]. The usual procedures give two constants of motion such as energy and the angular momentum of photons along the axis of symmetry and the mass as a third constant. However, in order to solve the system of equations, we need to define a fourth constant. The separability of the Hamilton–Jacobi equation enables us to obtain a fourth constant, which is the so-called Carter constant [43,44]. Despite defining the motivation for Hamilton–Jacobi formalism, we first need to describe the Lagrangian to obtain the relation between the constants of motion and the generalized momenta. In this case, the motion of a photon in the charged rotating WH space-time can be described by the

Lagrangian as

$$\mathcal{L} = \frac{1}{2}g_{ab}\dot{x}^a\dot{x}^b = -N^2\dot{t}^2 + \dot{r}^2\left(1 - \frac{b}{r} + \frac{Q^2}{r^2}\right)^{-1} + r^2K^2[\dot{\theta}^2 + \sin^2\theta(\dot{\phi} - \omega\dot{t})^2], \tag{5}$$

where “dot” defines the derivative with respect to affine parameter λ of the geodesic curves and the metric coefficients do not depend explicitly on time t and azimuthal angle ϕ . Hence, one can obtain the two conserved quantities such as [46]

$$p_t = \frac{\partial\mathcal{L}}{\partial\dot{t}} = -N^2\dot{t} - \omega r^2K^2\sin^2\theta(\dot{\phi} - \omega\dot{t}) = -E, \tag{6}$$

$$p_\phi = \frac{\partial\mathcal{L}}{\partial\dot{\phi}} = r^2K^2\sin^2\theta(\dot{\phi} - \omega\dot{t}) = L, \tag{7}$$

in which E and L are the energy and the angular momentum of photons, respectively. Now solving Eqs. (6) and (7), we obtain the expressions of \dot{t} and $\dot{\phi}$ as

$$\dot{t} = \frac{E - \omega L}{N^2}, \quad \dot{\phi} = \frac{L}{r^2K^2\sin^2\theta} + \omega\dot{t}. \tag{8}$$

Consequently, we obtained the components of r and θ of the momentum as

$$p_r = \frac{\partial\mathcal{L}}{\partial\dot{r}} = \frac{\dot{r}}{1 - \frac{b}{r} + \frac{Q^2}{r^2}}, \quad p_\theta = \frac{\partial\mathcal{L}}{\partial\dot{\theta}} = r^2K^2\dot{\theta}. \tag{9}$$

Equations (6) and (7) will be used in further calculations while dealing with the forms of generalized momenta and their relationship with the constants of motion. Particularly,

these equations will be helpful to write the system in terms of the constants E and L . The Hamilton–Jacobi equation is defined as

$$\frac{\partial S}{\partial \lambda} = -\frac{1}{2}g^{\mu\nu} \frac{\partial S}{\partial x^\mu} \frac{\partial S}{\partial x^\nu}, \tag{10}$$

where $g^{\mu\nu}$ is the inverse of the metric tensor and S is said to be Jacobi action, which is defined as [45,47]

$$S = \frac{1}{2}\mu^2\lambda - Et + L\phi + S_r(r) + S_\theta(\theta), \tag{11}$$

where $S_r(r)$ and $S_\theta(\theta)$ are unknown functions yet to be determined, μ is the mass of the test particle, which is zero for the photons. Here the Hamilton–Jacobi equation will be separable for the rotating WH as we choose in (1) if the metric functions N , b , K and ω only depend on radial coordinate r [47]. Now to get the equations for the functions $S_r(r)$ and $S_\theta(\theta)$, substitute Eq. (11) into Eq. (10), we obtain [47]

$$\left(\frac{dS_\theta}{d\theta}\right)^2 = \mathcal{K} - \frac{L^2}{\sin^2\theta}, \tag{12}$$

$$\left(1 - \frac{b}{r} + \frac{Q^2}{r^2}\right)N^2\left(\frac{dS_r}{dr}\right)^2 = (E - \omega L)^2 - \left(\mu^2N^2 + \mathcal{K}\frac{N^2}{r^2K^2}\right), \tag{13}$$

where \mathcal{K} is the Carter constant [44]. We know $p_r = \frac{\partial S}{\partial r} = \frac{dS_r}{dr}$ and $p_\theta = \frac{\partial S}{\partial \theta} = \frac{dS_\theta}{d\theta}$, therefore, Eqs. (9), (12) and (13) yield [47]

$$\frac{N}{\sqrt{1 - \frac{b}{r} + \frac{Q^2}{r^2}}} \frac{dr}{d\lambda} = \pm\sqrt{R(r)}, \quad r^2K^2\frac{d\theta}{d\lambda} = \pm\sqrt{T(\theta)}, \tag{14}$$

where

$$T(\theta) = \mathcal{K} - \frac{L^2}{\sin^2\theta}, \tag{15}$$

$$R(r) = (E - \omega L)^2 - \left(\mu^2N^2 + \mathcal{K}\frac{N^2}{r^2K^2}\right). \tag{16}$$

Then, the Jacobi action may be written in the following form

$$S = \frac{1}{2}\mu^2\lambda - Et + L\phi + \int \sqrt{\frac{R(r)}{N^2(1 - \frac{b}{r} + \frac{Q^2}{r^2})}}dr + \int \sqrt{T(\theta)}d\theta. \tag{17}$$

The constants of motions E , L , and \mathcal{K} are used as parameters for the geodesic equations in axisymmetric and stationary space-times. Hence, we introduce the dimensionless quantities such as

$$\xi = \frac{L}{E}, \quad \eta = \frac{\mathcal{K}}{E^2}, \tag{18}$$

where ξ and η are called the impact parameters. Further, the functions $R(r)$ and $T(\theta)$ can be written in terms of ξ and η as

$$R(r) = (1 - \omega\xi)^2 - \eta\frac{N^2}{r^2}K^2, \tag{19}$$

$$T(\theta) = \eta - \frac{\xi^2}{\sin^2\theta}. \tag{20}$$

3.1 The shadow of charged rotating traversable wormholes

The geodesic equations govern the motion of the particles and other objects in the gravitational fields of massive objects. Here, the particle under consideration is the photon, so the above equations describe the motion and the trajectories followed by the massless photon. Since we are studying the motion of photons in general, orbiting the WH in circular geodesics these photons stay on the surface of a sphere of radius $r = \text{constant}$. To find the WH shadow, i.e., the dark region in the viewer’s atmosphere in the presence of a shiny background, one would have to start finding out the critical orbits that separate the photons according to their motions around the WH. To perform this exercise, one can calculate the critical orbit by considering the radial geodesic equation, and it can be expressed as an energy conservation equation in the following form: [33]

$$\left(\frac{dr}{d\lambda}\right)^2 + V_{eff} = 1, \tag{21}$$

$$V_{eff} = 1 - \frac{1}{N^2}\left(1 - \frac{b}{r} + \frac{Q^2}{r^2}\right)R(r),$$

where V_{eff} is the effective potential that describes the geodesic motion of a photon around WH. From the above equation, we see that the motion of the photons depends on the impact parameter and the effective potential. Hence, one can analyze the motion of photons around WH, if its radial motion possesses a turning point $dr/d\lambda = 0$, which implies

$$V_{eff} = 1, \quad \frac{V_{eff}}{dr} = 0, \quad \frac{d^2V_{eff}}{dr^2} \leq 0. \tag{22}$$

We consider the explicit form of the V_{eff} and the functions N and $(1 - \frac{b}{r} + \frac{Q^2}{r^2})$ are finite and non-zero outside the WH throat. So, the conditions in Eq. (22) can be written as follows in terms of $R(r)$

$$R(r) = 0, \quad \frac{dR}{dr} = 0, \quad \frac{d^2R}{dr^2} \geq 0. \tag{23}$$

Thus, we can obtain the two algebraic equations for the impact parameters and the radial position of the unstable spherical orbit. In this scenario, by using the first two constraints of Eq. (23), we get the expressions for ξ and η in

terms of radial coordinate as following.

$$\xi = \frac{\chi}{\omega\chi - \omega'} \Big|_{r=r_{ph}}, \quad \chi = \frac{1}{2} \frac{d}{dr} \ln \left(\frac{N^2}{r^2 K^2} \right), \quad (24)$$

$$\eta = \frac{r^2 K^2}{N^2} (1 - \omega\xi)^2 \Big|_{r=r_{ph}}, \quad (25)$$

in which r_{ph} is the radius of circular photon orbit. In the above equations, we obtain the relation between impact parameters ξ and η as $\eta(\xi)$, and the prime denotes the derivative with respect to r . Using Eqs. (24) and (25), the authors in [47] discussed the WH shadows and exhibited that the effective potential has the maximum value at the WH throat, implying that the position of circular photon orbits, which is either stable or unstable, are lying at the WH throat. However, it has been shown that a WH throat can behave as a natural location of unstable circular orbits [42]. Hence, the condition $V_{eff} = 1$ is automatically satisfied. Therefore, for unstable circular orbits located at the WH throat such as $r = r_0$, the second condition in Eq. (22) can be written as [32]

$$(1 - \omega_0)^2 - \eta \frac{N_0^2}{r_0^2 K_0^2} = 0. \quad (26)$$

Next, we are going to discuss the distinct features of the free-moving matter around WH of the considering space-time geometry. Since the photons move on unstable orbits construct the edges of the shadow. Thus, the apparent shape of the shadow can be found by the projection of the shadow from the WH's plane to the observer's image plane with coordinates α and β . So, we introduce the celestial coordinates, that connected to the actual astronomical measurements that span a two-dimensional plane, defined as [48]

$$\alpha = \lim_{r_o \rightarrow \infty} \left(-r_o^2 \sin \theta_{obs} \left[\frac{d\phi}{dr} \right]_{(r_o, \theta_{obs})} \right), \quad (27)$$

$$\beta = \lim_{r_o \rightarrow \infty} \left(r_o^2 \left[\frac{d\theta}{dr} \right]_{(r_o, \theta_{obs})} \right), \quad (28)$$

where r_o is the position coordinate of the observer, lying far away from the WH, and θ_{obs} is the angular position of the observer with respect to the WH's plane. The celestial coordinates α and β are the discernible perpendicular distances of the shadow profiles as observed from the rotation axis and from its projection on the equatorial plane, respectively. Now, considering the geodesic equations, one can deduce explicit expressions for the celestial coordinates for our WH solution as

$$\alpha = -\frac{\xi}{\sin \theta_{obs}}, \quad \beta = \left(\eta - \frac{\xi^2}{\sin^2 \theta_{obs}} \right)^{1/2}. \quad (29)$$

The WH throat is considered at the origin of the image plane, see Fig. 3. Hence, the optical appearance of the WH shadow profiles formed by the unstable circular photon orbits that lie outside the throat are obtained through Eqs. (24), (25)

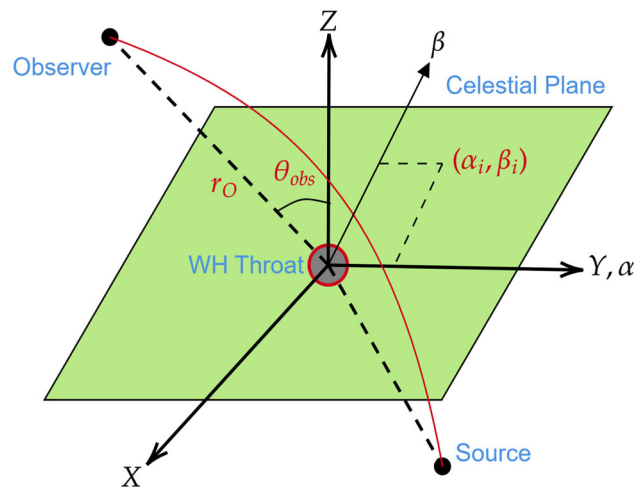


Fig. 3 Schematic diagram of the celestial coordinates for a distant observer

and (29) in the (α, β) plane. However, by using Eqs. (26) and (29), we get the solution for the part of the shadow's boundary, which can be formed due to the unstable circular orbits, located at WH throat as

$$(N_0^2 - \omega_0^2 r_0^2 K_0^2 \sin^2 \theta_{obs}) \alpha^2 - 2\omega_0 r_0^2 K_0^2 \sin \theta_{obs} \alpha - r_0^2 K_0^2 + N_0^2 \beta^2 = 0. \quad (30)$$

Therefore, based on Eq. (30), one can obtain the WH shadow images on the equatorial plane in the strong field regime with different values of model parameters. Further, to analyze the physical behavior of V_{eff} throughout the domain of WH geometry, one can choose the proper radial distance, which is explained by [8]

$$l(r) = \pm \int_{r_0}^r \frac{dr}{\sqrt{1 + \frac{Q}{r} - \frac{b}{r}}}, \quad (31)$$

here \pm corresponds to the asymptotic regions of universe I and universe II , respectively and the throat exists at $l(r_0) = 0$. To investigate the behavior of photons around WH, we first need to understand the physical behavior of effective potential. When the effective potential has the maximum value and reaches the position of the light ring, then the throat acts as a position of unstable photon orbits. Since the photons have non-zero angular velocity, they will revolve around the WH throat infinitely. Below, the maximum value of the effective potential, the photons lie away from the WH throat. Hence, at this position, the photons will encounter the potential barrier and travel throughout space-time freely. Further, above the position of the light ring, the photons approaching the throat from far away and continue moving in the inward direction, cross the WH throat from universe I and reach the photon orbit, from where it can either scatter back to infinity in the universe I or travel further into universe II [20, 49].

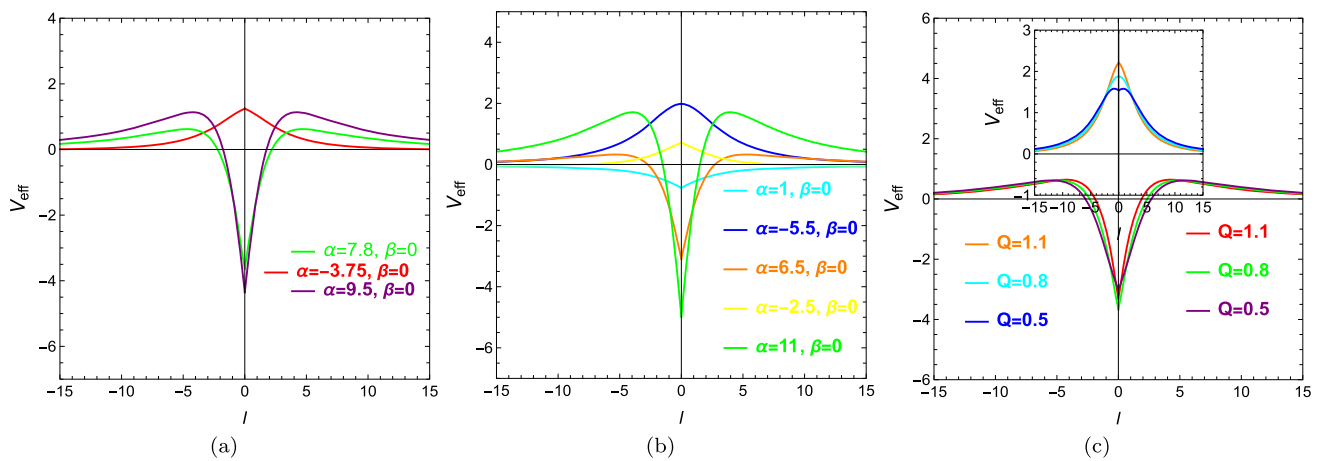


Fig. 4 The profiles of the effective potentials V_{eff} and l for different values of impact parameters and charge Q with $\theta_{obs} = \frac{\pi}{2}$

In this regard, from Eq. (21), we see that the motion of the particle depends on the impact parameters and the effective potential, which is depicted in Fig. 4, for different values of involved parameters. From Fig. 4, it is clear that the impact parameter values denoted by the different colors show that the corresponding curves of the effective potential for impact parameter values lying inside and outside of the WH throat, leads to different regions of the shadow boundary. If the effective potential has a turning point, i.e., $V_{eff} = 0$ at some value of $l(r)$ for the impact parameter values lying outside the shadow boundary. Photons with these impact parameters escape to the distant observer, thereby creating bright light spots in the observer's sky (see maroon and green curves of Fig. 4a). Further, in the case of the red curve in Fig. 4a), photons do not approach the WH throat and lie far away from it, since the light rays contribute negligible in creating the bright spot in the observer's sky. On the other hand, if the effective potential does not have any turning point, i.e., $V_{eff} \neq 0$ for the impact parameter lying inside the shadow boundary, photons with these impact parameters start their motion in the universe I , travel across the WH throat to universe II . These photons are not received by any distant observer, hence, creating a dark spot on the observer's sky (see the cyan curve of Fig. 4b). In a similar manner, one can also observe the behavior of the effective potential for some other values of parameters, see Fig. 4b, c, corresponding to the different positions of the photon orbit.

Now, we are going to examine the shadows observed by an observer in the vicinity of the WH for different values of parameters with $M = 1$. From Fig. 5a, it is found that with the increasing values of a , the shadow curves are shifted in the positive direction of abscissa. The inclusion of spin parameter a shifted the shadows rightwards and diminished flatness was observed with increasing a . In Fig. 5b, we see that with the increasing values of r_0 , the size of the shadow becomes more and more circular and it can be observed that each curve has

an almost equal magnitude of y , $-y$, x and $-x$ -intercepts, which means that the shadows are exactly circular. Further, in the case of charge Q , we see that as the value of charge Q increases, the size of each shadow curve decreases and shifts in the positive direction of abscissa, see Fig. 5c. Note that, in all cases of Fig. 5, the influence of each parameter can be observed clearly through differences in the shadow curves, which change significantly with the variations of parameters, and the overall shadow curves are shifted in the right direction due to the influence of a .

Next, we will interpret the shadow images of the WH at different positions of the observational angles. We investigate the effect of θ_{obs} on the WH shadow images for some particular values of model parameters as an example, see Fig. 6. From Fig. 6a, it can be seen that when $\theta_{obs} = \frac{\pi}{6}$, the image of the shadow is smaller, but as we increase the values of θ_{obs} , i.e., $\theta_{obs} = \frac{\pi}{2}$, we observed that the image size is also increased. Moreover, with an increase in the observational angle, the shadow image shifted rightwards and created a negligible flatness on the left side. As one goes from left to right in the panel, due to the variations of the parameters, the shadow size is changed accordingly. In Fig. 6b, c, a similar effect of θ_{obs} is found, as considered in the previous case. Further, it is essential to note that in similar circumstances, the differences between the shadow curves are smaller due to the decreasing values of Q (from left to right). However, in all cases, it is observed that with decreasing a in each panel (from left to right), the shadow images can be identified as perfect circles. These results are also consistent with the results in [47], however, the differences in positions of the photon orbit are found due to the influence of charge Q , which may be used to distinguish different types of WH shadow images under the considering framework.

In the next section, we are going to investigate the behavior of light rays near the WH [29, 51], which is the projection of the photon sphere on the equatorial plane.

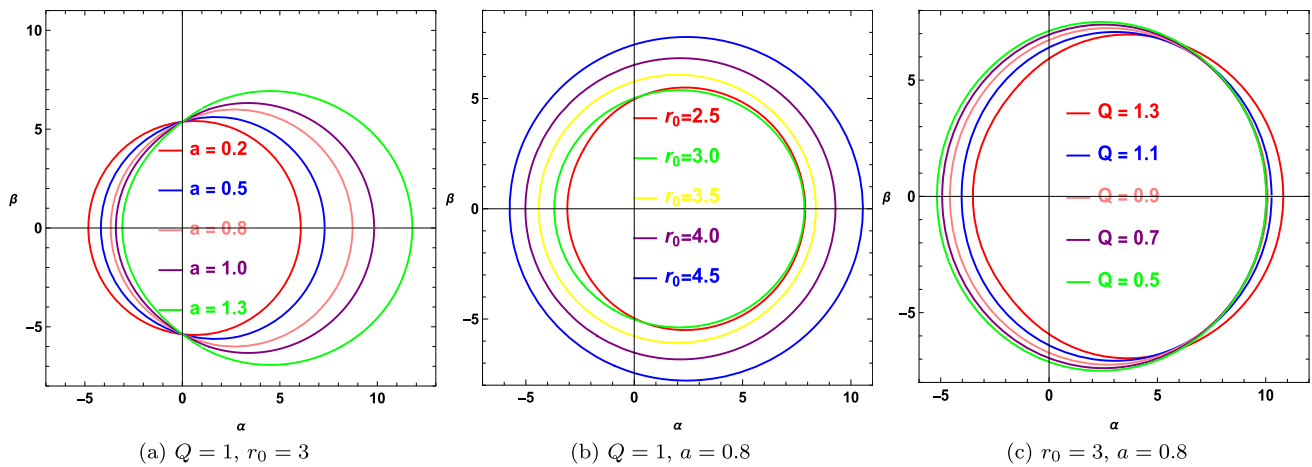


Fig. 5 The image of WH shadow is shown for different a , r_0 and Q in the left, middle, and right panels, respectively with $\theta_{obs} = \frac{\pi}{2}$

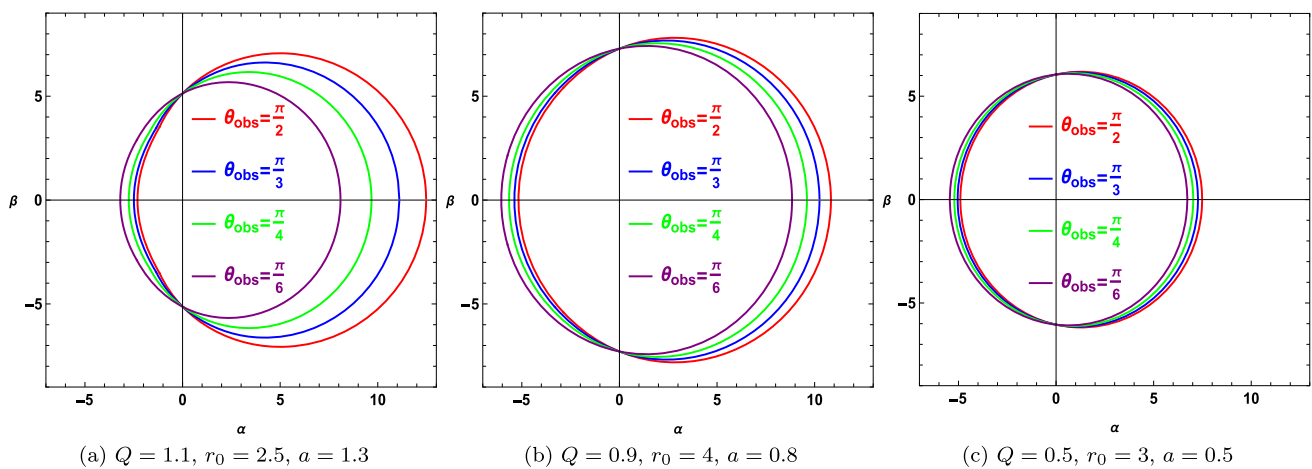


Fig. 6 The image of WH shadow is shown for different values of θ_{obs} (three examples are shown for different sets of parameters)

4 Behavior of light rays near the traversable wormhole

Recently, the research community has been motivated to explore the shadows cast by several compact objects when illuminated by different types of accretion disks. In this sense, they made some feasible assumptions that involved the many ingredients of accretion materials around the BH as well as WH space-time geometry [20,50,51]. The optical appearance of a WH’s shadow configuration may provide indirect evidence for the existence of the WH itself. Investigating, the size and the shape of the WH shadow, the scientific community infers the heuristic configurations of the WH such as its mass, spin, shape, and photon spheres because they are associated with the extreme warping dynamics of space-time geometry caused by massive objects. Moreover, the understanding of the existence and geometric properties of photon spheres around a TWH can help the scientific community to map the gravitational field of the WH in a strong regime,

which is crucial for understanding different types of accretion disks.

Based on these assumptions and along with the interest of reliable methods for visualizing the WH shadows with uniform brightness, we also consider this section an important part of our paper. In order to investigate the light deflection near the WH, the movement of light rays in this space-time needs to be understood. Since, the image on the observer’s screen is the gravitationally lensed trajectories of light rays coming from different parts of the sky, and hence it is convenient to understand the background geometry along the null geodesics of which photons would usually propagate [29,51,52]. In this perspective, we still use Eqs. (5)–(8), and impose the initial conditions $\theta = \frac{\pi}{2}$, $\dot{\theta} = 0$. That is, the light rays always move in the equatorial plane [46,51]. Further, we redefined the affine parameter as $\lambda \rightarrow \lambda/|L|$. Therefore, based on the null geodesics and the choices of the previous section, we obtain

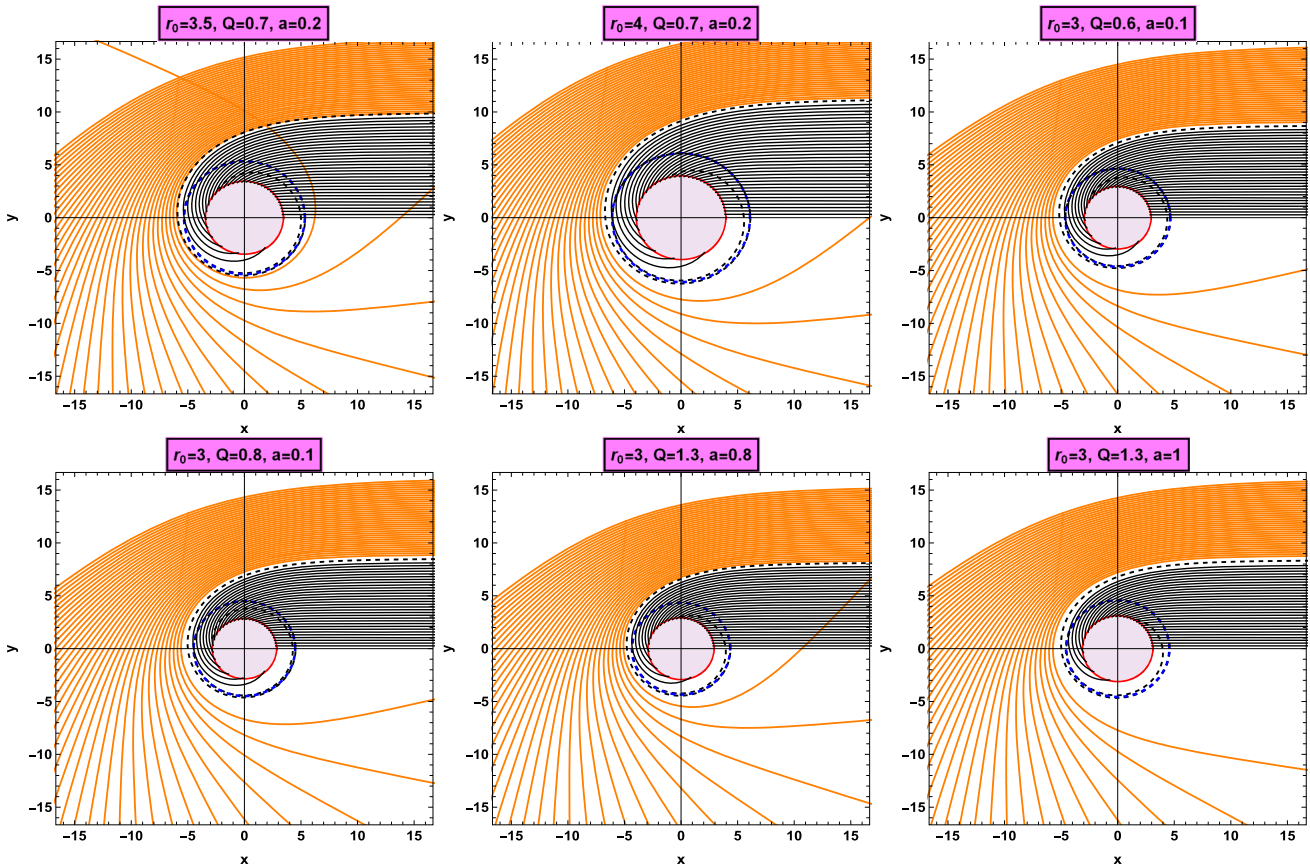


Fig. 7 Trajectories of light rays around a rotating TWH for different specific values of model parameters with $E = 1.2$ and $M = 1$. The coordinates here are given by $x = r \cos \phi$, $y = r \sin \phi$ and hence our terminology of light deflection refers to the polar coordinate ϕ .

The black dashed line, black lines, and orange lines correspond to the $\xi = \xi_{ph}$, $\xi < \xi_{ph}$, and $\xi > \xi_{ph}$ regions, respectively. The dashed blue line corresponds to the photon orbit while the red circumference indicates the WH’s throat radius

$$\frac{N^2 \dot{r}^2}{1 - \frac{b}{r} + \frac{Q^2}{r^2}} + \tilde{V}_{eff} = \frac{1}{\xi^2}, \tag{32}$$

where

$$\tilde{V}_{eff} = \frac{N^2}{K^2 r^2} + \frac{2\omega}{\xi} - \omega^2. \tag{33}$$

At the photon sphere, the motion of the light rays satisfies $\dot{r} = 0$ and $\ddot{r} = 0$ and obtain the radius of the photon sphere r_{ph} as

$$r_{ph} = \frac{\xi}{1 - \xi\omega} \frac{N}{K} \Big|_{r_{ph}}. \tag{34}$$

From Eq. (32), we see that the motion of the particle depends on the impact parameter ξ and the effective potential. Furthermore, the trajectory of the light ray can be depicted according to the equation of motion. Using Eqs. (6), (7) and (32), we have

$$\left(\frac{dr}{d\phi}\right)^2 = \frac{K^4 \left(1 - \frac{b}{r} + \frac{Q^2}{r^2}\right) \left(\frac{r^4(1-\xi\omega)^2}{N^2 \xi^2} - \frac{r^2}{K^2}\right)}{\left(1 + \frac{K^2 r^2 \omega(E-\omega)}{N^2}\right)^2}. \tag{35}$$

By setting $u = 1/r$, we can rewrite the Eq. (35) as

$$\begin{aligned} \left(\frac{du}{d\phi}\right)^2 &= \frac{K^4 \left(1 - bu + Q^2 u^2\right) \left(\frac{(1-\xi\omega)^2}{N^2 \xi^2} - \frac{u^2}{K^2}\right)}{\left(1 + \frac{K^2 \omega(E-\omega)}{u^2 N^2}\right)^2} \\ &= \Phi(u) \end{aligned} \tag{36}$$

The geometry of the geodesics depends on the roots of the equation $\Phi(u) = 0$. Utilizing the ray-tracing procedure, the trajectory of the light ray for different parameter values is shown in Fig. 7. One can find that each panel consists of a black dashed line, black lines, and orange lines, which correspond $\xi = \xi_{ph}$ (where ξ_{ph} is the impact parameter at photon sphere), $\xi < \xi_{ph}$, and $\xi > \xi_{ph}$, respectively. These pho-

ton trajectories with different colors represent three kinds of photon propagation in the rotating TWH space-time.

In addition, the location of the observer is important. Usually, the observer is located at an infinite boundary for the asymptotically flat space-time. We conveniently orientate our setup to locate the observer on the far right-hand side of the screen (corresponding to the north pole). When $\xi = \xi_{ph}$, the light rays will asymptotically approach the photon sphere and will revolve around the WH throat along the unstable circular orbit infinite times without perturbations; the light rays with $\xi > \xi_{ph}$ will encounter the potential barrier and then be scattered to infinite after passing through the turning point, which is determined by the equation $\Phi(u) = 0$, where $\Phi(u)$ has been defined in Eq. (36). The light rays with $\xi < \xi_{ph}$ move in the inward direction and are absorbed by the BH eventually. This kind of light ray cannot be received by the distant observer, so a shadow forms in the observational sky. Further, we also analyze the influence of each parameter on the behavior of light rays such as the position of the photon orbit, and the throat size, which changed significantly according to variation of parameters. For instance, we plotted the left and middle panels of Fig. 7 (see top row) for the fixed values of charge $Q = 0.7$ and $a = 0.2$, while varying the throat radius as $r_0 = 3.5$ and $r_0 = 4$, respectively. It is found that the radius of the WH throat increases with increasing r_0 , and the light rays are more gentle near the throat for larger r_0 (see left and middle panel of top row). Moreover, we also calculate the values of the impact parameter $\xi_{ph} = 9.93$ and $\xi_{ph} = 11.22$ for the left and middle panels of the top row, respectively, leading to a change in the position of the photon orbit, as shown in the blue dashed circumference around the WH throat. In a similar manner, we plotted the shadow images for some other values of parameters, (see the remaining panels of Fig. 7). The optical appearance of the shadow images is like those of the above discussion as there are multiple winding of light rays close to the photon orbit, which is hard to distinguish. However, the differences are observed in the positions of the photon ring, WH throat size, and the behavior of light rays, which is found sensitive corresponding to each value of the parameter.

4.1 Observed intensities

In the previous section, we have observed the shadow of the WH as the central depression of the image as seen by any distant observer, these are highly idealized observables, while realistic astrophysical images are mainly fueled by the physics of the accretion disk around compact object. A precise modeling of this problem requires the use of general relativistic magneto-hydrodynamic simulations because these simulations relevant to the EHT observations provided the most suitable scenario [53]. However, significant progress can also be made on the theoretical front through the ana-

lytical models of accretion disks with a localized emission on a given geodesic. In this perspective, we investigate the specific intensity observed by the distant observer, which is defined as [54,55]

$$I = \int g^3 j(v_{em}) dl_{prop}, \tag{37}$$

in which $g = v_o/v_{em}$ is the red-shift factor, v_o is the observed photon frequency and v_{em} is the emission frequency of the photon, $j(v_{em})$ represents the emission per unit volume measured in the static frame of the emitter and dl_{prop} is the infinitesimal proper length. For rotating TWH, the red-shift factor has a value $g = (N^2 r^2 K^2 \omega^2)^{1/2}$. In addition, we assume that the radiation of light is monochromatic with fixed frequency ν_t , i.e.,

$$j(v_{em}) \propto \frac{\delta(v_{em} - \nu_t)}{r^2}, \tag{38}$$

where we have adopted $1/r^2$ profile as used in [55]. The proper length in the rest frame of the emitter can be calculated as

$$dl_{prop} = \left(\frac{1}{1 - \frac{b}{r} + \frac{Q^2}{r^2}} + r^2 K^2 \left(\left(\frac{d\phi}{dr} \right)^2 - 2\omega \frac{d\phi}{dr} \frac{dt}{dr} \right) \right)^{1/2} dr, \tag{39}$$

in which $\frac{d\phi}{dr}$ is given by Eq. (35). Further, the specific intensity observed by the static observer is

$$I = - \int d\phi u'(\phi) \left(N^2 - \frac{K^2 \omega^2}{u^2} \right)^{3/2} \left(\frac{1}{1 - bu + Q^2 u^2} + K^2 u^2 \left(1 - \frac{2\omega}{\omega + \frac{u^2 N^2}{K^2(E-\omega)}} \right) \right)^{1/2}. \tag{40}$$

Figure 8 shows the observed intensity I as a function of impact parameter ξ for some specific values of model parameters. As intensity depends on the behavior of light rays associated with the impact parameter ξ , we need to analyze how intensity changes with respect to the impact parameter ξ . From Fig. 8 (top row), we observed that the intensity first ascended and reached a peak at ξ_{ph} , and then dropped to lower values with increasing ξ . When $\xi < \xi_{ph}$, the intensity comes from the accretion and is mostly absorbed by WHs. When $\xi = \xi_{ph}$, the light rays revolve around the WH many times and hence, the optical path is infinite. Thus, a distant observer sees the strongest luminosity at the position of the photon ring. After that, when $\xi > \xi_{ph}$, only the refracted light participates in the observer's intensity. Further, as the value of ξ increases, the refracted light starts to obtain smaller values and disappears when ξ approaches infinity. Moreover, the

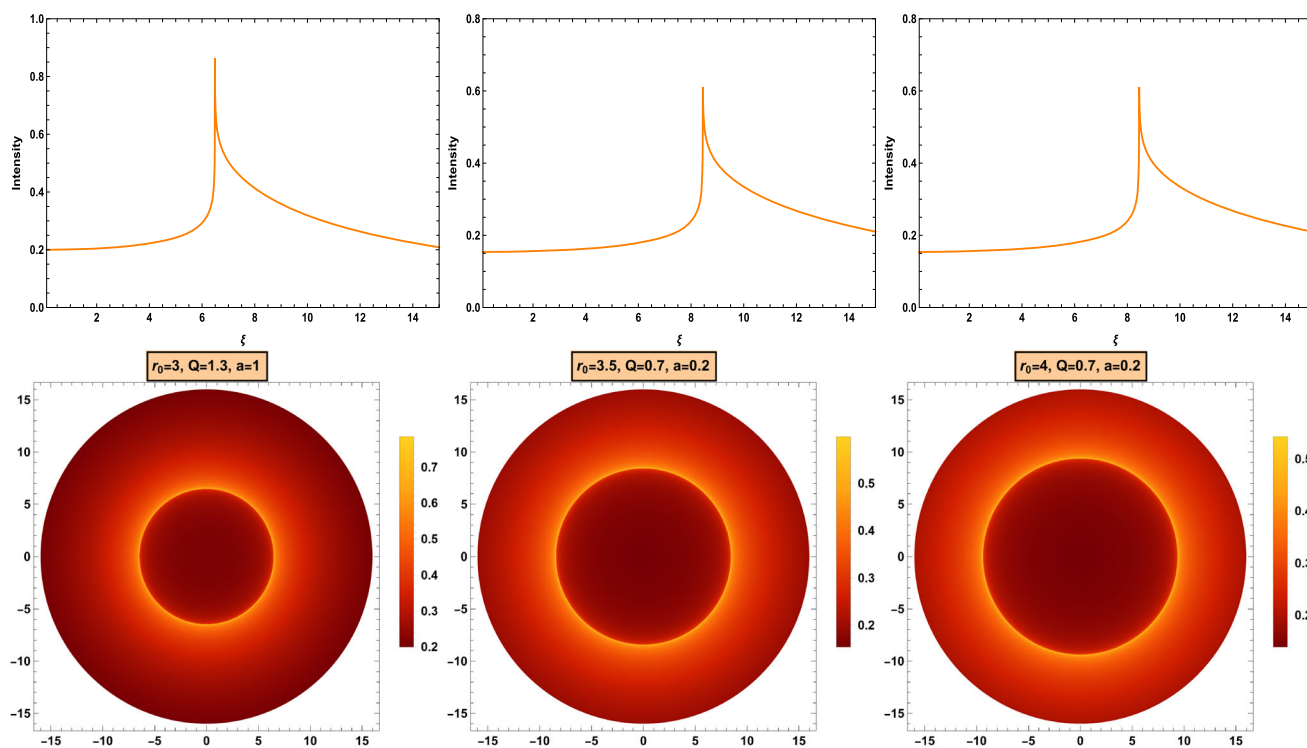


Fig. 8 Profiles of the observed specific intensity seen by a distant observer for a static spherical accretion under some specific values of model parameters with $E = 1.2$ and $M = 1$ (three examples are shown).

The bottom panels depicted the optical appearance of the observed specific intensity in two-dimensional density maps in celestial coordinates

peak value of the intensity at $\xi = \xi_{ph}$ should be approached to infinity because the light ray revolved around the WH many times and depicted the arbitrary maximum intensity. However, due to the numerical approximations and the logarithmic type of the intensity, the actual computed intensity never approaches infinity, as argued in [20]. Moreover, from the top row of Fig. 8, one can also observe how the involved parameters affect the observed intensity in each panel. The lower row of Fig. 8 shows corresponding two-dimensional density maps of the shadows in the celestial coordinates. From this, one can observe that there is a bright photon ring (which is the photon sphere) surrounds a central dark region. Further, inside the photon sphere, we notice that the shadow is not a completely dark region with zero intensity since the perspective of the shadows seen by any distant observer is occupied by the photons that have escaped from the bright accretion flow. Moreover, the radii of the photon spheres are found to be different in each panel of Fig. 8. Particularly, one can see from left to right panels of Fig. 8 that with increasing r_0 , the radii of the photon spheres also increase. In addition, the total luminosity of the charged rotating TWH shadow also increases from left to right panels of Fig. 8 with variation in parameters.

5 Concluding remarks

In the last few years, testing horizonless compact objects with light rings has become increasingly popular among the scientific community, particularly after the beginning of multi-messenger astronomy. Because these objects can be potential alternatives to BHs and can be laboratories for testing modifications to GR at the horizon scale. The year 2019 brought to our weaponry the analysis of BH shadows, theoretically, the central depression to a bright ring of radiation bounded by a critical curve, a beautiful picture that must be significantly upgraded when the features of the main source of illumination are provided by the accretion disk surrounding the BHs or WHs as well. It is therefore important to investigate the numerous physical properties of these objects and see whether or how we can distinguish these objects from BHs through observations or theoretical points of view [50]. To this end, strong gravitational lensing is an important observational tool for probing the space-time geometries around these objects, where the optical appearance of the photon sphere provides significant information about space-time dynamics. In the present study, we have investigated the shadows cast by charged rotating TWHs. We have stud-

ied in detail why and how the throat of a charged rotating TWH plays a crucial role in shadow formation, which is constructed in strong gravitational lensing. The analytical method is adopted for shadow study starting with Hamilton–Jacobi formalism and then applying the celestial coordinates to observe the shadow curves on the observer’s screen. Furthermore, using the ray-tracing procedure, we have also analyzed the light trajectories on the equatorial plane with different colors, representing three kinds of photon propagation in the WH space-time. Lastly, the shadows and photon rings of charged rotating TWH with static spherical accretions are discussed and the corresponding two-dimensional density maps are obtained on the observational plane with celestial coordinates. The results presented with the description of figures are summarized below:

- Figure 2 illustrates that the ergoregion extends across the horizon and to the throat. Explicitly from left to right, as the strength of the spin parameter a increases, the distance between the ergosurface and the WH throat is expanded. Further, we plotted the ergosphere for different values of Q , corresponding to the obtained values of spin parameter a . We can see that as the value of Q decreases from left to right, the corresponding profiles show that the distance between the ergosurface and the WH throat is gradually expanded (see the bottom panel of Fig. 2). It is obvious that all these results are qualitatively different from the previous studies [33] due to the influence of charge Q .
- In Fig. 4, we depicted the effective potential for several values of parameters. When α has positive values, the effective potential starts from inside the throat and immediately increases to a maximum value and then decreases on both sides with respect to l . These results imply that effective potential has a turning point, i.e., $V_{eff} = 0$ at some l , photons with these impact parameters escape to the distant observer, thereby creating bright spots in the observer’s sky. In particular, when $\alpha = 1$, the effective potential does not have any turning, i.e., $V_{eff} \neq 0$, photons with these impact parameters enter into WH throat, passing through it and go to the other side of the throat. These photons are not received by any distant observer, and hence observer will see a dark spot on the screen. On the other hand, when α has negative values, the effective potential lies far away from the throat, here the photons approaching the throat from far away may reach the throat or be reflected. Furthermore, we found a similar behavior of the effective potential for different values of charge Q , as we discussed for positive and negative values of α .
- Using geodesic equations, we have plotted the shadow images of WH observed by any distant observer in Fig. 5. It is found that the spin parameter shifts the shadow to the right and a possible flatness is observed. Further, the increasing values of r_0 also increase the shadow radius and circular symmetry can be identified in all cases. The increase in charge Q decreases the size of the shadow and shifts to the left with decreasing Q .
- The difference in shadows due to effect of θ_{obs} is observed in Fig. 6. The higher values of θ_{obs} increase the difference between the shadow curves and shift rightwards accordingly. However, by decreasing a from left to right, the shadow circles gradually move to the left side. All these results imply that space-time parameters affect the size and symmetry of the WH shadow significantly.
- Based on the ray-tracing method, we illustrated the optical appearance of the light trajectories near the WH region in Fig. 7. The corresponding plots show that the size of the WH throat, photon ring, and light curves show different observational appearances corresponding to each value of the state parameters. These solutions are qualitatively similar with [29, 51], but there are some differences in the sizes and locations as well as in the contributions to the total luminosity of the different light rings induced by the TWH configurations, they are hardly a viable candidate to interpret the massive object discovered at the center of the M87 Milky Way galaxy by the EHT collaboration.
- The observed specific intensity of WH shadows is depicted in Fig. 8 when it is illuminated by the static spherical accretion flows. We found that the observed intensity ascended first sharply with the increasing of ξ , reached the peak position at the photon orbit, and then gradually decreased. In all cases, we notice that there is a bright ring outside the central dark region, the size and position of the photon ring dramatically changed with respect to the state parameters. These findings imply that the WH shadow size depends on the space-time parameters and the shadow’s luminosities rely on the accretion flow model.

Based on our analysis, we conclude that the above discussion may provide fruitful results for the theoretical study of the WH shadow profiles and their relevant dynamics. The results found in this paper point out that distinguishing between WHs and BHs based on their light rings and shadows would be challenging because both objects could produce similar optical appearances in these aspects. Further, WHs are still under consideration as their theoretical investigations are not well-defined in the same way as BHs, which have been widely studied in astrophysics, as numerous notable publications have been devoted to the analysis of BH shadows and their theoretical constraints in the context of GR and modified theories of gravity as well. To distinguish between them and for minimum uncertainties, of course, some new ideas, more observations, and highly precise systematic implementation of this issue would require investigating, illustrating the well-defined optical appearance of the accretion’s disk

on the observer's screen and geometrical properties as well as their dynamical behavior [50]. Recently, the motion of photons, neutral and charged particles around WH described by exponential metric, which is the solution of the Einstein-scalar field equations has been investigated in [56]. These results reveal that some interesting aspects of shadow radii and photon spheres in the space-time described by the exponential metric may shed some deep insights into the behaviors of particles and gravitational lensing effects near the WHs. Further, some interesting aspects of WH structures are also discussed in [57], for example, the shadows with two photon spheres allow an observer on one of the sides of the WH to see another shadow in addition to the one generated by its own photon sphere, which is due to the photons passing above the maximum of the effective potential on its side and bouncing back across the throat due to a higher effective potential on the other side, which can be capable to yield additional light rings on the equatorial plane.

In a word, with the advancement of observational technology, such as Baseline Interferometry observations by the EHT collaboration, an increasing number of shadow images of massive objects will be obtained soon. To potentially distinguish different types of objects, more theoretical investigations need to be under consideration. Our present study predicts new possible images describing the optical appearance of rotating TWHs, which might be observable in the future. Since rotating objects are considered to be more realistic in the universe, we expect that these results inspire the theoretical study of WH shadow images and other physical quantities that may be fruitful for the observational teams working on achieving high resolution of the photon sphere and WH configurations in GR and modified theories of gravity as well. Another direction could also be considered a more realistic environment around the rotating WHs, such as shadows from geometrically and optically thin accretion disks with three toy models, transfer functions, and free-falling matter, which might be considered to modify our present analysis. We leave this as a future investigation.

Acknowledgements We are grateful to Dr. Rajibul Shaikh for his valuable discussions and support in completing this article.

Data availability All data generated or analyzed during this study are included in this published article.

Open Access This article is licensed under a Creative Commons Attribution 4.0 International License, which permits use, sharing, adaptation, distribution and reproduction in any medium or format, as long as you give appropriate credit to the original author(s) and the source, provide a link to the Creative Commons licence, and indicate if changes were made. The images or other third party material in this article are included in the article's Creative Commons licence, unless indicated otherwise in a credit line to the material. If material is not included in the article's Creative Commons licence and your intended use is not permitted by statutory regulation or exceeds the permitted use, you will need to obtain permission directly from the copy-

right holder. To view a copy of this licence, visit <http://creativecommons.org/licenses/by/4.0/>.
Funded by SCOAP³.

References

1. E. Gourgoulhon et al., Gravitational waves from bodies orbiting the Galactic Center black hole and their detectability by LISA. *Astron. Astrophys.* **627**, A92 (2019)
2. R. Abuter et al., Detection of the Schwarzschild precession in the orbit of the star S2 near the Galactic centre massive black hole. *Astron. Astrophys.* **636**, L5 (2020)
3. K. Akiyama, et al., First *M87* event horizon telescope results. I. The shadow of the supermassive black hole. *Astrophys. J. Lett.* **875**, L1 (2019)
4. C. Winkler et al., The Integral mission. *Astron. Astrophys.* **411**, L1 (2003)
5. P. Soffitta et al., XIPE: the X-ray imaging polarimetry explorer. *Exp. Astron.* **36**, 523 (2013)
6. L. Flamm, Republication of: Contributions to Einstein's theory of gravitation. *Gen. Relativ. Gravit.* **47**, 72 (2015)
7. A. Einstein, N. Rosen, The particle problem in the general theory of relativity. *Phys. Rev.* **48**, 73 (1935)
8. M.S. Morris, K.S. Thorne, Wormholes in spacetime and their use for interstellar travel: a tool for teaching general relativity. *Am. J. Phys.* **56**, 395 (1988)
9. S. Hawking, G. Ellis, *The Large Scale Structure of the Spacetime* (Cambridge University Press, Cambridge, 1973)
10. E. Teo, Rotating traversable wormholes. *Phys. Rev. D* **58**, 024014 (1998)
11. P. Kuhfittig, Axially symmetric rotating traversable wormholes. *Phys. Rev. D* **67**, 064015 (2003)
12. K. Akiyama et al., First *M87* event horizon telescope results. II. Array and instrumentation. *Astrophys. J. Lett.* **875**, L2 (2019)
13. Akiyama, K. et al., First *M87* event horizon telescope results. III. Data processing and calibration. *Astrophys. J. Lett.* **875**, L3 (2019)
14. Akiyama, K. et al., First *M87* event horizon telescope results. IV. Imaging the central supermassive black hole. *Astrophys. J. Lett.* **875**, L4 (2019)
15. D. Psaltis, Gravitational test beyond the first post-Newtonian order with the shadow of the *M87* black hole. *Phys. Rev. Lett.* **125**, 141104 (2020)
16. S.I. Kruglov, The shadow of *M87* black hole within rational non-linear electrodynamics. *Mod. Phys. Lett. A* **35**, 2050291 (2020)
17. H. Falcke, F. Melia, E. Agol, Viewing the shadow of the black hole at the galactic center. *Astrophys. J.* **528**, L13 (1999)
18. R. Takahashi, Black hole shadows of charged spinning black holes. *Publ. Astron. Soc. Jpn.* **57**, 273 (2005)
19. A. Abdujabbarov et al., Shadow of Kerr-Taub-NUT black hole. *Astrophys. Space Sci.* **344**, 429 (2013)
20. S.E. Gralla, D.E. Holz, R.M. Wald, Black hole shadows, photon rings, and lensing rings. *Phys. Rev. D* **100**, 024018 (2019)
21. X.X. Zeng, M.I. Aslam, R. Saleem, The optical appearance of charged four-dimensional Gauss-Bonnet black hole with strings cloud and non-commutative geometry surrounded by various accretions profiles. *Eur. Phys. J. C* **83**, 129 (2023)
22. R. Saleem, M.I. Aslam, Observable features of charged Kiselev black hole with non-commutative geometry under various accretion flow. *Eur. Phys. J. C* **83**, 257 (2023)
23. R. Takahashi, Shapes and positions of black hole shadows in accretion disks and spin parameters of black holes. *Astrophys. J.* **611**, 996 (2004)

24. A. Saha, S.M. Modumudi, S. Gangopadhyay, Shadow of a non-commutative geometry inspired Ayón-Beato and García black hole. *Gen. Relativ. Gravit.* **50**, 103 (2018)
25. J. Solanki, V. Perlick, Photon sphere and shadow of a time-dependent black hole described by a Vaidya metric. *Phys. Rev. D* **105**, 064056 (2022)
26. A. Övgün et al., Shadow cast of noncommutative black holes in Rastall gravity. *Mod. Phys. Lett. A* **35**, 2050163 (2020)
27. M. Visser, Traversable wormholes: the Roman ring. *Phys. Rev. D* **55**, 5212 (1997)
28. K.A. Bronnikov, R.A. Konoplya, T.D. Pappas, General parametrization of wormhole spacetimes and its application to shadows and quasinormal modes. *Phys. Rev. D* **103**, 124062 (2021)
29. H. Huang et al., Light ring behind wormhole throat: geodesics, images, and shadows. *Phys. Rev. D* **107**, 104060 (2023)
30. M. Guerrero et al., Shadows and optical appearance of black bounces illuminated by a thin accretion disk. *J. Cosmol. Astropart Phys.* **08**, 036 (2021)
31. P.G. Nedkova, V.K. Tinchev, S.S. Yazadjiev, Shadow of a rotating traversable wormhole. *Phys. Rev. D* **88**, 124019 (2013)
32. R. Shaikh, Shadows of rotating wormholes. *Phys. Rev. D* **98**, 024044 (2018)
33. F. Rahaman et al., Shadows of Lorentzian traversable wormholes. *Class. Quantum Gravity* **38**, 215007 (2021)
34. A. Abdujabbarov et al., Shadow of rotating wormhole in plasma environment. *Astrophys. Space Sci.* **361**, 226 (2016)
35. M. R., Neto, D. Perez, J. Pelle, The shadow of charged traversable wormholes. *Int. J. Mod. Phys. D* **32**, 2250137 (2023)
36. W. Javed, A. Hamza, A. Övgün, Weak deflection angle by Casimir wormhole using Gauss–Bonnet theorem and its shadow. *Mod. Phys. Lett. A* **35**, 2050322 (2020)
37. T. Ohgami, N. Sakai, Wormhole shadows in rotating dust. *Phys. Rev. D* **94**, 064071 (2016)
38. M.A. Bugaev et al., Gravitational lensing and wormhole shadows. *Astron. Rep.* **65**, 1185 (2021)
39. P.M. Takisa, S. Ray, S.D. Maharaj, Charged compact objects in the linear regime. *Astrophys. Space Sci.* **350**, 733 (2014)
40. S.W. Kim, H. Lee, Exact solutions of a charged wormhole. *Phys. Rev. D* **63**, 064014 (2001)
41. P.H.R.S. Moraes, W. De Paula, R.A.C. Correa, Charged wormholes in $f(R, T)$ extended theory of gravity. *Int. J. Mod. Phys. D* **28**, 1950098 (2019)
42. R. Shaikh et al., A novel gravitational lensing feature by wormholes. *Phys. Lett. B* **789**, 270 (2019)
43. S. Chandrasekhar, *The Mathematical Theory of Black Holes* (Oxford University Press, Oxford, 1983)
44. B. Carter, Global structure of the Kerr family of gravitational fields. *Phys. Rev.* **174**, 1559 (1968)
45. S. Dastan, R. Saffari, S. Soroushfar, *Eur. Phys. J. Plus* **137**, 1002 (2022)
46. X.X. Zeng et al., QED and accretion flow models effect on optical appearance of Euler–Heisenberg black holes. *Eur. Phys. J. C* **82**, 764 (2022)
47. P.G. Nedkova, V. Tinchev, S.S. Yazadjiev, Shadow of a rotating traversable wormhole. *Phys. Rev. D* **88**, 124019 (2013)
48. I. Bray, Kerr black hole as a gravitational lens. *Phys. Rev. D* **34**, 367 (1986)
49. M. Guerrero et al., Shadows and optical appearance of black bounces illuminated by a thin accretion disk. *J. Cosmol. Astropart Phys.* **2021**, 036 (2021)
50. M. Guerrero et al., Light ring images of double photon spheres in black hole and wormhole spacetimes. *Phys. Rev. D* **105**, 084057 (2022)
51. T. Tangphati et al., Shadows and photon spheres in static and rotating traversable wormholes. [arXiv:2310.16916](https://arxiv.org/abs/2310.16916) [gr-qc]
52. V.A. De Lorenci et al., Light propagation in non-linear electrodynamics. *Phys. Lett. B* **482**, 134 (2000)
53. R. Gold et al., Verification of radiative transfer schemes for the EHT. *Astrophys. J.* **897**, 148 (2020)
54. M. Jaroszynski, A. Kurpiewski, Optics near Kerr black holes, spectra of advection dominated accretion flows. *Astron. Astrophys.* **326**, 419 (1997)
55. C. Bambi, Can the supermassive objects at the centers of galaxies be traversable wormholes? The first test of strong gravity for mm/submm very long baseline interferometry facilities. *Phys. Rev. D* **87**, 107501 (2013)
56. B. Turimov, Y. Turaev, B. Ahmedov, Z. Stuchlík, Circular motion of test particles around wormhole represented by exponential metric. *Phys. Dark Universe* **35**, 100946 (2022)
57. M. Guerrero, G.J. Olmo, D. Rubiera-Garcia, Double shadows of reflection-asymmetric wormholes supported by positive energy thin-shells. *J. Cosmol. Astropart. Phys.* **04**, 066 (2021)